# The nanoscale organization of the Nipah virus fusion protein informs new membrane fusion mechanisms.

Qian Wang[1], Jinxin Liu[1], Yuhang Luo[1], Vicky Kliemke[1], Giuliana Leonarda Matta[1], Jingjing Wang[1], Qian Liu[1,2,*]

[1] Institute of Parasitology, Faculty of Agricultural and Environmental Sciences, McGill University, Saint Anne de Bellevue, Canada.

[2] McGill Center for Viral Diseases, Lady Davis Institute, Montreal, Canada.

## Abstract.

Paramyxovirus membrane fusion requires an attachment protein for receptor binding and a fusion protein for membrane fusion triggering. Nipah virus (NiV) attachment protein (G) binds to ephrinB2 or -B3 receptors, and fusion protein (F) mediates membrane fusion. NiV-F is a class I fusion protein and is activated by endosomal cleavage. The crystal structure of a soluble GCN4-decorated NiV-F shows a hexamer-of-trimer assembly. Here, we used single-molecule localization microscopy to quantify the NiV-F distribution and organization on cell and virus-like-particle membranes at a nanometer precision. We found that NiV-F on biological membranes forms distinctive clusters that are independent of endosomal cleavage or expression levels. The sequestration of NiV-F into dense clusters favors membrane fusion triggering. The nano-distribution and organization of NiV-F are susceptible to mutations at the hexamer-of-trimer interface, and the putative oligomerization motif on the transmembrane domain. We also show that NiV-F nanoclusters are maintained by NiV-F-AP-2 interactions and the clathrin coat assembly. We propose that the organization of NiV-F into nanoclusters facilitates membrane fusion triggering by a mixed population of NiV-F molecules with varied degrees of cleavage and opportunities for interacting with the NiV-G/receptor complex. These observations provide insights into the in-situ organization and activation mechanisms of the NiV fusion machinery.

## Introduction.

The family of *Paramyxoviridae* contains many clinically important viruses, such as human parainfluenza virus 1-3, measles virus, and Nipah virus (NiV). Paramyxoviruses code for two glycoproteins on the viral membranes for virus-cell membrane fusion. The receptor-binding proteins (RBP, HN/H/G) engage the host receptors and activate the refolding of the fusion protein (F) that merges the virus and cell membranes[1]. Paramyxovirus-F is a class I fusion protein, along with human immunodeficiency virus (HIV) envelope, influenza virus hemagglutinin, and severe acute respiratory syndrome coronavirus-2 (SARS-CoV-2) spike[1]. Paramyxovirus-F is a trimeric transmembrane protein with a “tree-like” structure at its prefusion conformation. Upon triggering by the RBP/receptor complex, paramyxovirus-F mediates fusion by inserting its N-terminal fusion peptides into the target membrane and undergoes a conformational change from pre- to post-fusion conformations, similarly to other class I fusion proteins. The refolding of the paramyxovirus-F overcomes the energy barrier for membrane fusion and leads to virus-cell and cell-cell membrane fusion.

NiV is a well-studied paramyxovirus due to its capability of human-human and human-animal transmissions, high mortality and morbidity rates, and the unavailability of vaccines or therapeutics for human use[2,3]. NiV is closely related to Hendra virus, Cedar virus, and the newly identified Langya virus[4]. NiV-F is expressed on the cell surface as an fusion-inactive form,

activated in the endosome by cathepsin B and L cleavage, and exocytosed to the cell surface as a fusion-active form[5,6]. NiV-G binds to ephrinB2 and/or -B3 receptors in host cells and triggers the refolding of F that leads to virus-cell membrane fusion[7]. Three complementary models of the NiV fusion activation mechanism have been proposed in the past. *In the first model*, the NiV-G and F form a complex before receptor engagement. The F/G interaction maintains F at a prefusion conformation. The receptor binding to G induces conformational changes in G, leading to the release and refolding of F. This model is supported by co-immunoprecipitation and conformational antibody binding assays[8,9]. *In the second model*, NiV-F exists as hexamer-of-trimers, and the fusion peptides are sequestered at the hexameric interface. The activation of one single trimer by the NiV-G/ephrinB2 complex can be transmitted to all six trimers via the interfaces of the hexamer-of-trimers, leading to efficient F-triggering and fusion pore formation. This model is supported by the crystal structure of a GCN4-decorated NiV-F ectodomain and mutagenesis analysis of key amino acid residues at the hexameric interfaces[10]. *In a third model*, NiV-F and G do not form a complex before receptor binding. The NiV-G/ephrinB2 engagement clusters ephrinB2 and triggers F. F triggering leads to reduced mobility of a portion of F molecules that potentially contributes to fusion pore formation. This model is supported by the nanoscale distribution of NiV-F and G on cell membranes resolved by super-resolution microscopy and a single-particle tracking assay of NiV fusion protein at the interface between supported lipid bilayer and live cell membranes[11,12]. Although these models explain the NiV membrane fusion mechanisms from different perspectives, a link between the molecular structure and the fusion machinery on biological membranes remains unclear.

We attempted to address this link by analyzing the nano-organization of NiV-F at the prefusion state on biological membranes using single-molecule localization microscopy (SMLM) and mutagenesis analyses. We have shown that NiV-F forms clusters on biological membranes that are isolated from NiV-G[11]. Here, we show that NiV-F forms regular-sized nanoclusters on cell membranes regardless of the expression level or endosomal cleavage. The estimated size of NiV-F clusters on cell membrane is similar to that of the hexamer-of-trimer assemblies formed by the GCN4-decorated soluble NiV-F. The NiV-F nano-organization is altered by mutations at the hexameric interface and the putative oligomerization motifs at the transmembrane domain. NiV-F molecules enriched in nanoclusters favor membrane fusion activation. The NiV-F nanoclusters are stabilized by the interactions between NiV-F, the endocytosis adaptor complex AP-2, and the clathrin coat at the cell membranes. In summary, our study reveals the NiV-F nano-organization on the biological membranes and provides novel insights into the NiV fusion machinery *in situ*.

**NiV-F forms regular-sized clusters that are not affected by the surface expression level.**

We recently published that NiV-F formed distinctive nanoclusters on the plasma membrane regardless of the presence of NiV-G or ephrinB2[11]. To investigate the determinants of the NiV-F nano-organization, we used SMLM to probe the NiV-F at various conditions. SMLM generates super-resolution images by localizing spatially far-apart fluorophores with nanometer precision[13]. PK13 cells have a flat morphology that is suitable for SMLM imaging. PK13 cells express little endogenous ephrinB2 and -B3 receptors for NiV and thus can eliminate any potential receptor-dependent clustering. Cell surface NiV-F was detected using a FLAG tag in its extracellular domain[11]. The FLAG tags were employed to detect NiV-F because of the availability of high affinity and specificity anti-FLAG antibodies for a high labeling density, which is vital for the reconstruction accuracy of SMLM images[14]. To rule out the effect of the FLAG tag

on NiV-F clustering, we compared NiV-F clusters formed by NiV-F-FLAG to that of a NiV-F-HA construct. Both HA and FLAG tags were inserted after amino acid residue 104, right before the fusion peptide (Fig. S1A). Visual examination of the SMLM images reveals that NiV-F-FLAG and NiV-F-HA form similar clusters (Fig. S1B). The clustering tendency, indicated by Hopkins' index, is comparable between NiV-F-HA and NiV-F-FLAG (Fig. S1C), suggesting that NiV-F clustering is not affected by specific epitope tags. To test whether the FLAG tag affects the function of NiV-F, we pseudotyped NiV-G-HA and NiV-F-FLAG or un-tagged NiV-F on the recombinant vesicular stomatitis virus (VSV) with glycoprotein (G) replaced by a *Renilla* luciferase gene (VSV-ΔG-rluc) and determined the viral entry levels (VSV/NiV pseudoviruses). The virus entry induced by NiV-F-FLAG is comparable to that of untagged NiV-F (Fig. S1D), verifying that the FLAG tag has minimal effect on the membrane fusion activity of NiV-F.

Next, we investigated whether the nano-organization of NiV-F depends on the cell surface expression levels. The total cell surface expression level (CSE) of NiV-F in a selected cell was measured before the cell was subjected to SMLM imaging. The SMLM images show that NiV-F forms similar nanoclusters in both high-expression and low-expression cells (Fig. 1A and B). Our data show that the clustering tendency of NiV-F is independent of its CSE in individual cells (Fig. 1C). To gain a quantitative understanding of NiV-F nanoscale organization, we used a cluster identification method DBSCAN (Density-Based Spatial Clustering of Applications with Noise) that links the closely situated localizations in a propagative manner. We created cluster and density maps using Clus-DoC for representative high-expression and low-expression cells (Fig. 1D and E)[15]. Our data show that the estimated diameter of the NiV-F clusters ranges from 20-34 nm, with a peak at 24 nm (Fig. 1F). Nonetheless, the precise values of the cluster diameter are indicative rather than definite in SMLM as it could be affected by the labeling complex and the blinking property of the fluorophore. The distribution of the cluster diameter shows that ~60% of NiV-F clusters have similar sizes, indicating that NiV-F clusters maintain a quite uniform appearance. Interestingly, we noticed that the size of the clusters (Fig. 1G) and localization density (Fig. 1H) in clusters were similar between high- and low-expression cells, suggesting that the NiV-F organization in nanoclusters is not affected by the expression levels. Moreover, our data show that the high-expression cells have more clusters than the low-expression cells (Fig. 1I). These results suggest that changes in CSE may affect the number of NiV-F clusters on the plasma membrane (Fig. 1I), but not the clustering tendency of NiV-F (Fig. 1C), the size of the clusters (Fig. 1G), or the localization density within clusters (Fig. 1H). These data imply that the distribution and nano-organization of NiV-F are tightly regulated and may be important for membrane fusion activation. We also analyzed NiV-F distribution in different cell lines. HeLa cells express ephrinB2 and -B3, and thus are NiV permissive cells. The overall NiV-F nano-organization seems quite similar on PK13 and HeLa cells, agreeing with our previous results (Fig. S2A)[11]. The Hopkins' indices are also similar for NiV-F on PK13 and HeLa cells (Fig. S2B). The DBSCAN analysis shows that the percentage localizations in clusters (Fig. S2C), the relative density defined as the ratio of the localization density in clusters to the total localization density in the selected region (Fig. S2D), and cluster diameters (Fig. S2E) are comparable for NiV-F on PK13 and HeLa cells. These results suggest that NiV-F clusters are minimally affected by the cell lines of expression or the presence of the ephrinB2 and/or -B3.

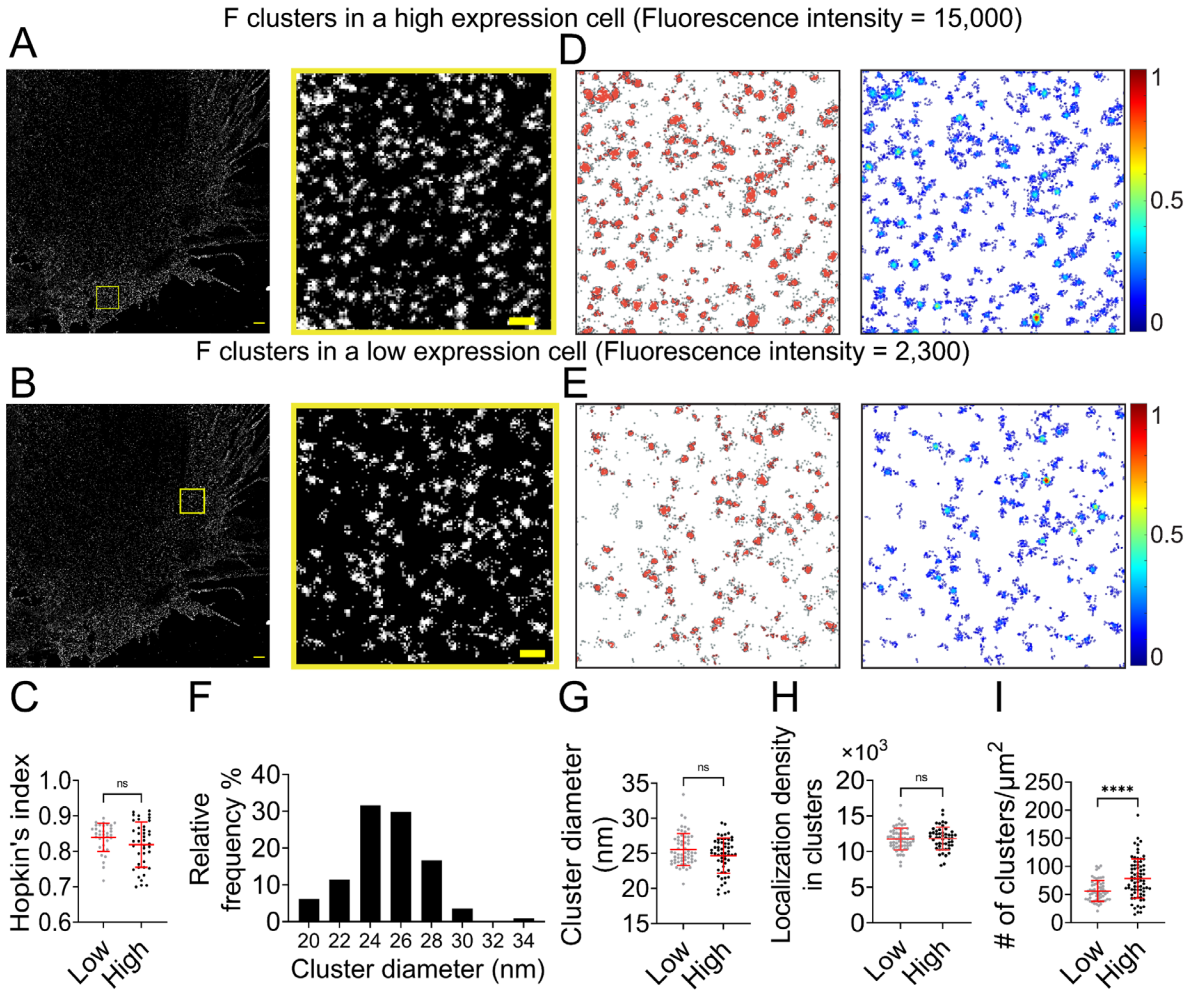


***Fig. 1. NiV-F forms regular-sized clusters that are not affected by the surface expression level****. (A and B) Cross-section (Δz = 600 nm) of SMLM images of NiV-F in high-expression (A) and low-expression (B) PK13 cells. Scale bar: 1 μm. The yellow boxed region is enlarged to show the detailed distribution pattern. Scale bar: 0.2 μm. (C) Hopkin's index of the F localizations in low- and high-expression cells. n = 35 and 40. (D and E) Cluster maps (left) and localization density maps (right) of the enlarged regions in A and B. Cluster contours are highlighted with gray lines. Normalized relative density is pseudocolored according to the scale on the right. (F) The percentage distribution of the NiV-F cluster diameter from 13 cells. n = 133. (G) The cluster diameters in low- and high-expression cells. n = 58 and 56. (H) The localization density (# of localizations per μm$^2$) within clusters in low- and high-expression cells. n = 58 and 50. (I) The number of clusters per μm$^2$ in low- and high-expression cells. n = 59 and 74. The cut-off fluorescence intensity for low- and high-expression cells is 8000 (Arb. Unit). Sample size n is the number of total regions from 6-8 cells. Bars represent mean ± SD. P value was obtained using the Mann-Whitney test. ns: p > 0.05; * p<0.01; ** p<0.001; *** p<0.0001.*

**The NiV-F nanoclusters are not affected by NiV-F cleavage.**

NiV-F is synthesized in host cells as inactive precursor $F_0$ and cleaved by cellular proteases cathepsin L and cathepsin B in the endosomes at an acidic pH to generate the fusion-active, disulfide-linked $F_1$-$F_2$ construct. The $F_1$-$F_2$ is subsequently recycled to the cell surface to induce

cell-cell fusion and incorporated into virus particles. We hypothesized that the $F_0$ precursor and the $F_1$-$F_2$ active forms co-existed in the same clusters on the cell surface. To test this hypothesis, we used a pan-cysteine cathepsin inhibitor E64d to inhibit the NiV-F cleavage. E64d inhibited the cell-cell fusion induced by NiV-F and NiV-G in HeLa cells (Fig. S3), agreeing with the previous fusion inhibitory effects in Vero and MDCK cells[5,6]. Our SMLM images show that E64d treatment does not result in any significant change in the clustering of NiV-F in HeLa cells (Fig. 2A). The clustering extent of NiV-F was not altered by the E64d treatment, as shown by comparable Hopkin's indices (Fig. 2B). Additionally, quantitative parameters of the nano-organization such as percentage of localizations in clusters (Fig. 2C), relative density (Fig. 2D), cluster size (Fig. 2E), and the total density of the regions (Fig. 2F) were comparable. Our data show that clusters formed by non-cleaved NiV-F in cells treated by E64d are similar to those formed by a mixture of cleaved and non-cleaved NiV-F in the control cells, suggesting that F cleavage does not alter F clustering on the cell membrane. These data support our hypothesis that the non-cleaved precursor $F_0$ and cleaved $F_1$-$F_2$ coexist in the same cluster on the cell membrane.

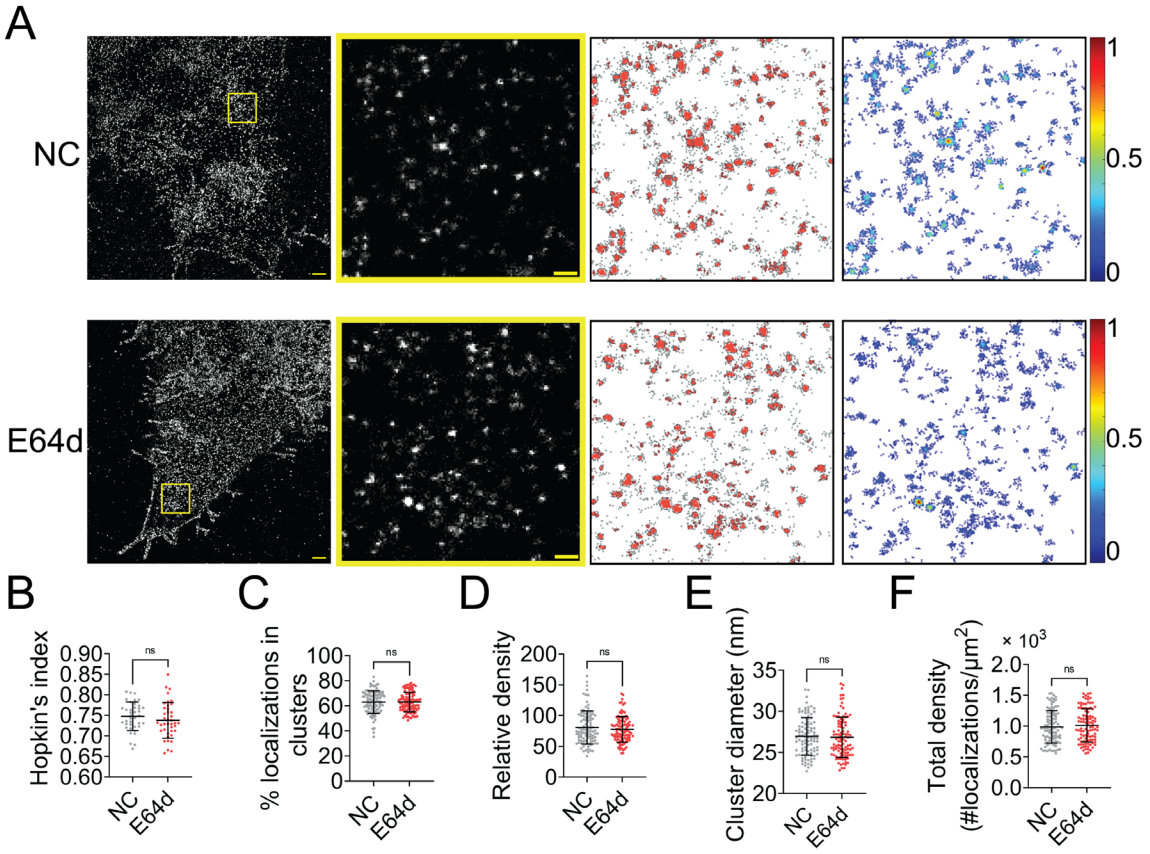


***Fig 2. Endosomal cleavage does not affect the nanoscale distribution of NiV-F.*** *(A) First column: Cross-section (Δz = 600 nm) of SMLM images of NiV-F in HeLa cells untreated (NC) and treated with 20 μM E64d (E64d). HeLa cells were co-transfected by expression plasmids coding for NiV-G and NiV-F. Twenty μM E64d or the same volume of solvent methanol was added to cells at 2 hrs post-transfection. Scale bar: 1 μm. Second column: The yellow boxed region in the first column is enlarged to show individual clusters. Scale bar: 0.2 μm. Third column: Cluster maps from the enlarged regions. Fourth column: Localization density maps*

*show the normalized relative density of the enlarged regions. (B-F) Quantitative analyses of NiV-F clusters formed in HeLa cells without (NC) and with (E64d) the E64d treatment: (B) Hopkin's index, n = 40 and 40; (C) percentage of localizations in clusters, n = 101 and 101; (D) relative density, n = 100 and 103; (E) average cluster diameters, n = 100 and 101; (F) total density of the region, n = 101 and 102. Bars represent mean ± SD. p value was obtained using Mann-Whitney test. ns: p > 0.05; * p<0.01; ** p<0.001; *** p<0.0001. Sample size n is the number of total regions from 4-10 cells.*

**Mutations destabilizing the NiV-F hexamer-of-trimer assembly alter its nano-organization on the plasma membrane.**

We noticed that the uniformity in the NiV-F cluster morphology resembled the hexameric assembly of soluble NiV-F decorated by GCN4[10]. Next, we investigated whether NiV-F clusters were stabilized by the hexameric interface. As reported, L53D and V108D mutants destabilize the hexameric interface and demonstrate decreased membrane fusion ability; Q393L stabilizes the hexameric interface and demonstrates increased fusion ability[10]. We inserted the FLAG tag into the ectodomains of these mutants at the same position as that of the NiV-F. We verified that the relative fusion ability to their F-WT counterpart was comparable between the FLAG-tagged and untagged mutants (Fig. S4A and S4B)[10]. The FLAG-tagged mutants showed similar CSE levels to NiV-F (Fig. S4C). All mutants showed some levels of processing, although the cleavage of L53D was the least efficient compared to F-WT and other mutants (Fig. S4D). Additionally, the FLAG-tagged NiV-F mutants showed a similar trend in virus entry as that of cell-cell fusion when pseudotyped to a recombinant VSV virus (Fig. S4E and S4F), agreeing with the previous results obtained using the NiV-F constructs with a C-terminal AU1 tag[10]. We also generated VLPs expressing NiV-M-β-lactamase (NiV-M-Bla), NiV-G-HA, and NiV-F-FLAG or mutants for an entry kinetics assay. The entry kinetics was measured in real-time by conversion of green to blue fluorescence resulting from CCF2-AM dye cleavage by the β-lactamase upon the entry of VLPs[16,17]. Our results show that the hyperfusogenic mutant Q393L shows more efficient VLP entry than that of WT, while VLPs bearing the hypofusogenic mutant L53D and V108D are less efficient in entry than that of the WT (Fig. S4G and S4H). It is noteworthy that the incorporation of NiV-G seems to be impacted by the expression of L53D in both VSV/NiV pseudovirions and VLPs (Fig. S4F and S4H), and the deficient virus entry induced by L53D may be partly due to the decreased attachment to the target cells (Fig. S4E and S4G). Nonetheless, the level of L53D on the pseudovirions and VLPs seems comparable to that of the WT (Fig. S4F and S4H). These data support that mutations at the hexameric interface significantly impact the fusion activity of NiV-F on both cell and virus surface.

NiV-F mutants L53D, V108D, and Q393L were expressed on PK13 cells and subjected to SMLM imaging. The images show that clusters formed by L53D and V108D are smaller and more dispersed than those of the F-WT and Q393L (Fig. 3A). The Hopkin's index for Q393L is significantly higher than that of F-WT, while the Hopkin's indices for L53D and V108D are slightly lower than that of F-WT (Fig. 3B). Consistently, a lower percentage of L53D and V108D localizations are segregated into clusters than that of F-WT, while a similar percentage of Q393L and F-WT localizations form clusters (Fig. 3C). In addition, clusters of L53D and V108D are less packed than that of F-WT, with 48-, 49-, and 55-fold denser than the total localization density in the region, respectively (Fig. 3D). The clusters of Q393L are not significantly denser than that of F-WT (Fig. 3D). Our analysis also shows that L53D and V108D form smaller clusters compared to the F-WT (Fig. 3E). The Q393L clusters are of a similar size to that of F-WT (Fig. 3E). The

total density of localizations and the total CSE levels for all constructs are comparable (Fig. 3F and Fig. S4C), suggesting that differences in clustering are not due to variable numbers of localizations or levels of expression. Collectively, these data show that the mutations destabilizing the hexameric interface (L53D and V108D) make NiV-F localizations more dispersed and form smaller and less packed clusters. Q393L that stabilizes the hexameric interface promotes the clustering of NiV-F localizations (Fig. 3B) but does not significantly alter the organization and morphology of individual clusters (Fig. 3C-F). These data suggest that the NiV-F clusters are susceptible to mutations at the hexameric interface. Considering that the uniformed cluster size is similar to the assemblies formed by the soluble GCN4-NiV-F, we propose that NiV-F may organize into hexamer-of-trimer on the plasma membrane.

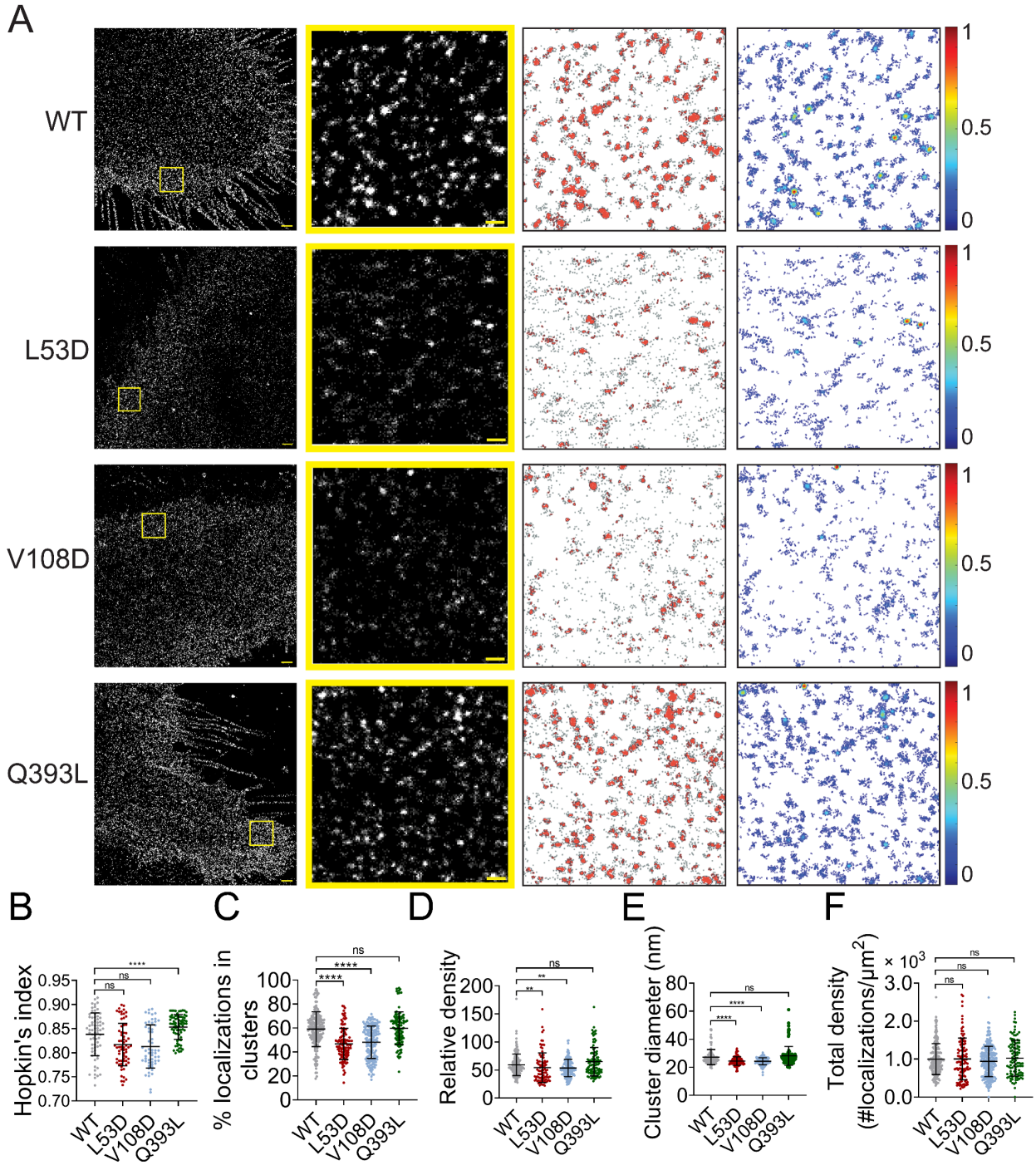


***Fig. 3. Mutations at the NiV-F hexameric interface affect its nano-organization****. (A) First column: Cross-section (Δz = 600 nm) of SMLM images of the FLAG-tagged NiV-F-WT (WT), L53D, V108D, and Q393L on PK13 cell membrane. Scale bar: 1 μm. Second column: The yellow boxed regions in the first column are enlarged to show individual clusters. Scale bar: 0.2 μm. Third column: Cluster maps from enlarged regions. Fourth column: Localization density maps show normalized relative density of the enlarged regions. (B-F) Quantitative analyses of the distribution of the FLAG-tagged NiV-F constructs: (B) Hopkin's index, n = 57-70; (C) Percentage of localizations in clusters, n = 106-198; (D) Relative density, n = 90-187; (E)*

*Average cluster diameters, n = 106-196; (F) total density of the region (a ratio of total localizations in a region to the size of the region), n = 105-242. Bars represent mean ± SD. Sample size n is the number of total regions from 11-20 cells. p value was obtained using Mann-Whitney test. ns: p > 0.05; * p<0.01; ** p<0.001; *** p<0.0001.*

**Mutations at the NiV-F hexameric interface affect its distribution on the VLP membrane.** To further investigate the organization of F mutants in viral membranes, we imaged the FLAG-tagged NiV-F constructs on VLPs produced by 293T cells expressing NiV-M-GFP, NiV-G, and NiV-F-WT, L53D, V108D, or Q393L mutants. The incorporation of NiV-F is comparable among the NiV-F constructs (Fig. 4A). The L53D and V108D on VLPs are less cleaved compared to that of the F-WT and Q393L, as suggested by the weaker NiV-$F_2$ bands (Fig. 4A). Notably, the incorporation of NiV-G is largely abrogated in the VLPs that expressing L53D (Fig. 4A).

To probe the organization of NiV-F constructs on VLPs, the F-constructs on VLP membranes were stained using Alexa Fluor 647 and subjected to SMLM imaging. The GFP fluorescence on NiV-M was used to locate the VLPs. Fig. 4B shows that F-WT and F-Q393L form distinctive clusters, while localizations of L53D and V108D are more dispersed on a z = 100 nm projection. This agrees with their distributions on the plasma membrane (Fig. 3A). To gain a quantitative insight into the distribution of the F constructs on the three-dimensional (3D) VLPs, we used an algorithm named OPTICS (Ordering Points To Identify Clustering Structure)[18]. To identify clusters, the OPTICS algorithm sorts out the localizations by calculating the reachability distance between two adjacent localizations in a propagative manner and generates a sequence of the ordered localizations[18]. In the plot of reachability distance vs. the sequence of ordered localizations, a sudden increase in the reachability distance marks the cutoff of a cluster (Fig. S5A). The shade between neighboring peaks represents localizations that are classified in one cluster (Fig. S5A). OPTICS can identify sub-clusters on a 3D VLP that may not be recognized by DBSCAN that uses one fixed parameter for the entire dataset. Fig. S5B shows the OPTICS plots of the localizations of F-WT and mutants on representative VLPs (Fig. 4B). The noticeable kinks suggest that F-WT and Q393L form distinctive clusters on VLPs, while the irregular, small kinks indicate that L53D and V108D are more dispersed and form smaller clusters on VLPs (Fig. 4B and Fig. S5B). To gain a population insight on the nano-organization of the F constructs on VLPs, we developed a one-dimensional convolutional neural network (1D CNN) to classify the ordered sequence of reachability distances of the NiV-F localizations obtained by the OPTICS algorithm[19]. The distribution patterns of the localizations of the F-WT and Q393L partition into one category, and L53D and V108D in another (Fig. 4C). These results indicate that L53D and V108D form smaller and more dispersed clusters than F-WT and Q393L on the VLP membranes, agreeing with that of the plasma membrane (Fig. 3). Our results indicate that the trimer-trimer interaction at the hexameric interface is key in stabilizing the nano-organization of NiV-F on both cell and viral membranes, and NiV-F do not seem to rearrange during the incorporation into VLPs. Nonetheless, our data do not rule out the possibility that the association of nucleocapsids with the plasma membrane during assembly may reorganize NiV-F on the authentic virus membranes. Since the incorporation levels of NiV-M and -G varies among mutants, the nano-organization of NiV-F is likely associated with the virion incorporation or budding.

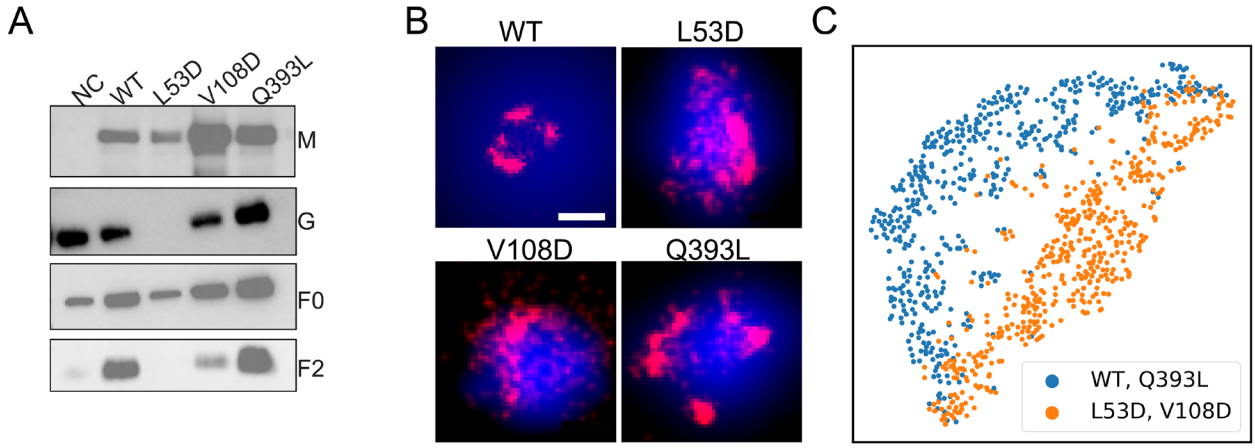


***Fig. 4. The distribution and organization of NiV-F constructs in VLPs.*** *(A). The incorporation of F-WT and mutants in VLPs. NiV-M-GFP, G-HA, and FLAG-tagged F-WT or mutants were transfected to 293T cells. The supernatants were collected at 48 hrs post-transfection and analyzed on SDS-PAGE followed by western blotting. NiV-M was probed by polyclonal goat anti-GFP, NiV-G polyclonal rabbit anti-HA, $F_0$ and $F_2$ M2 monoclonal mouse anti-FLAG antibody. (B) Cross-section (Δz = 100 nm) of SMLM images of the FLAG-tagged NiV-F-WT (WT), L53D, V108D, and Q393L on individual VLPs. Scale bar: 0.2 μm.* (C) The classification of the ordered sequence of reachability distances of the NiV-F constructs localizations. Orange: F-WT (n = 306) and Q393L (n = 323); Blue: L53D (n = 310) and V108D (n = 329). n is the number of VLPs used for classification analysis.

**The NiV-F clusters are dispersed upon the disruption of the interactions between transmembrane domains (TMD).** Evidence shows that TMD of class I fusion protein can self-associate in the absence of the rest of the protein and is important for membrane fusion[20]. Previous studies show that mutations in the Leucine-Isoleucine Zipper (LI zipper) motif lead to the dissociation of an HeV-F TMD-derived peptide, decreased stability, and the fusion ability of the whole HeV-F protein[21]. As the TMD domains of the NiV- and HeV-F demonstrate a 94% similarity, we mutated leucine (488 and 509) and isoleucine (495 and 502) residues of the LI zipper in NiV-F TMD to alanine (LI4A) (Fig. S6A). Similar to their counterparts of HeV-F, the NiV-F-LI4A showed a decreased F processing (Fig. S6B), cell-cell fusion activity (Fig. S6C and S6D), and CSE levels (Fig. S6E)[21]. The NiV-F-LI4A failed to incorporate into VSV/NiV pseudovirions (Fig. S6F), and thus did not induce any virus entry (Fig. S6G). Visual inspection of the images suggests that LI4A forms bigger clusters than F-WT (Fig. 5A). However, the LI4A seems less likely to cluster than F-WT, indicated by a lower Hopkin's index (Fig. 5B). Similarly, the portion of LI4A localizations partitioned into clusters is slightly lower than that of WT (Fig. 5C). Interestingly, we noticed that clusters formed by LI4A are significantly bigger (Fig. 5D) than that of F-WT and with a similar localization density within the clusters (Fig. 5E). The data suggest that interactions between TMDs of NiV-F monomers play a role in stabilizing its nano-organization. Dissociation of TMDs by mutations may result in increased space between F monomers and thus leads to bigger clusters on the cell membrane.

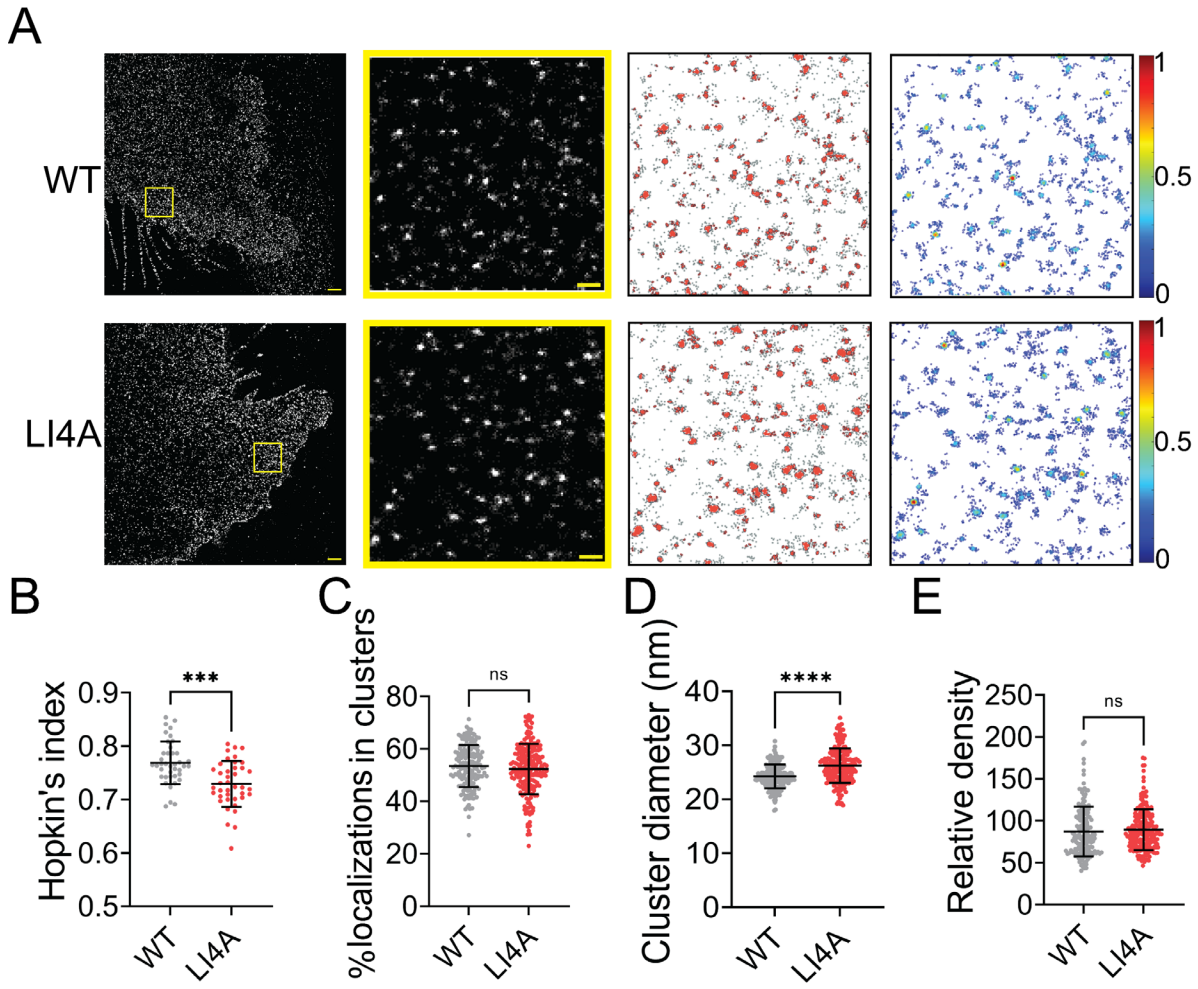


***Fig. 5. Mutations in the LI zipper of the NiV-F transmembrane domain disturbs the NiV-F distribution.*** *A) First column: Cross-section (Δz = 600 nm) of SMLM images of the FLAG-tagged NiV-F-WT (WT) and NiV-F-LI4A (LI4A) mutant on PK13 cell membrane. Scale bar: 1 µm. Second column: The yellow boxed region in the first column is enlarged to show individual clusters. Scale bar: 0.2 µm. Third column: Cluster maps from enlarged regions. Fourth column: Localization density maps show normalized relative density of the enlarged regions in the second column. (B-E) Quantitative analyses of the WT and LI4A clusters: (B) Hopkin's index, n=40 and 40 (C) Percentage of localizations in clusters, n = 171 and 211; (D) Average cluster diameters, n = 171 and 211; (E) Relative density, n = 166 and 211. Bars represent mean ± SD. p value was obtained using Mann-Whitney test. ns: p > 0.05; * p<0.01; ** p<0.001; *** p<0.0001. Sample size n is the number of total regions from 13-16 cells.*

**The NiV-F nanoclusters are stabilized by endocytosis components**.

NiV-F can be endocytosed for endosomal cleavage. Next, we investigated whether NiV-F clusters are stabilized during endocytosis. NiV-F contains an endocytosis sorting signal YSRL and an additional YY motif at its cytoplasmic tail (Fig. S7A). Mutation of these tyrosine residues to alanine almost diminished NiV-F cleavage[6]. A FLAG-tagged NiV-F-YA construct containing the aforementioned mutations resulted in significantly less $F_2$ band than F-WT (Fig. S7B) and

completely abrogated cell-cell fusion in 293T cells (Fig. S7C and S7D), although the CSE levels were comparable to that of F-WT (Fig. S7E). The YA mutant did not incorporate into the VSV/NiV pseudovirions (Fig. S7F) and thus did not mediate virus entry (Fig. S7G). By visually inspecting the SMLM images, we noticed that F-YA was less clustered than that of F-WT (Fig. 6A). Indeed, the Hopkin's analysis suggests that F-YA is less clustered than F-WT (Fig. 6B). The DBSCAN analysis shows that lower percentage of F-YA localizations segregate into clusters (Fig. 6C) than that of the F-WT, and clusters formed by F-YA are smaller (Fig. 6D) and less dense (Fig. 6E) than that of the F-WT. Notably, there is no significant difference in the total density for F-YA and F-WT SMLM images (Fig. 6F), indicating that the differences in cluster organizations do not result from overall protein expression or the stochastic blinking properties of the fluorophore. These results suggest that the endocytosis sorting signal of NiV-F may facilitate the enrichment of NiV-F into clusters on the cell surface, preparing them for endosomal cleavage and/or incorporation into viruses.

It is established that the YxxΦ sorting signal on the endocytosis cargo is bound and enriched by the heterotetrameric adaptor protein (AP) complexes, which further recruit the assembly of the clathrin coat[22,23]. We hypothesize that the clustering of NiV-F is promoted by the assembly of the clathrin coat via the NiV-F-AP-2 interactions. As suggested by a yeast two-hybrid analysis, NiV-F interacts with μ1, μ2, μ3 and μ4 subunits of the AP complexes AP-1, AP-2, AP-3, and AP-4, and mutations of Y525, Y542, and Y543 almost completely abolished the interaction between AP-2 and NiV-F[24]. Indeed, the co-immunoprecipitation assay shows that less AP2μ2 is pulled down by F-YA than that of F-WT, suggesting that F-YA has a reduced interaction with AP-2 (Fig. S7H). Next, we examined the NiV-F clusters in HeLa cells treated by the endocytosis inhibitor pitstop2. Pitstop2 blocks clathrin-mediated endocytosis by obstructing the binding of the accessory protein (*e.g.* AP-2) and the clathrin terminal domain, and potentially preventing the assembly of the clathrin coat[25]. The SMLM images (Fig. 6G) show that the NiV-F localizations are more dispersed upon pitstop2 treatment, agreeing with the lower Hopkin's index (Fig. 6H) and a smaller percentage of localizations in clusters (Fig. 6I) in pitstop2 treated group compared to that of the control group. Interestingly, we noticed that the NiV-F clusters in pitstop2 treated cells were larger than the control cells (Fig. 6J), although with similar densities (Fig. 6K). The total density is consistent between the pitstop2 treated and control groups (Fig. 6L). The overall dispersed NiV-F distribution upon pitstop2 treatment may potentially be caused by the disrupted assembly of clathrin coat. In combination, these results suggest that the enrichment of NiV-F by AP-2 and the subsequent assembly of the clathrin-coated endosomes are important in stabilizing the F clusters on cell membranes. We envision that the endocytosis components may also facilitate the NiV-F clustering in virus particles as previous proteomic studies show the presence of endocytosis related proteins, such as clathrin, AP-2, and dynamin in NiV VLPs[26–28].

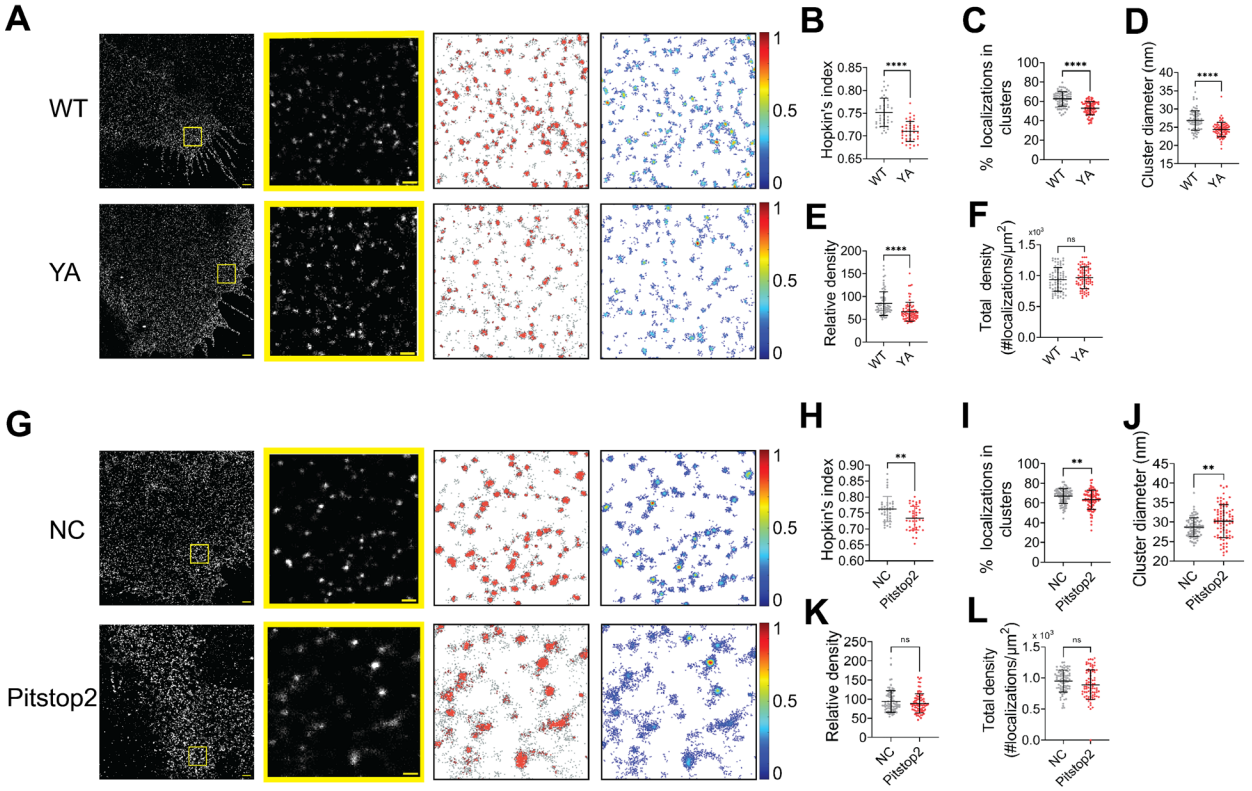


***Fig. 6. The NiV-F nanoclusters are stabilized by endocytosis components.*** *(A) First column: Cross-section (Δz = 600 nm) of SMLM images of the FLAG-tagged NiV-F-WT (WT) and NiV-F-YA (YA) mutant on PK13 cell membrane. Scale bar: 1 μm. Second column: The yellow boxed region in the first column is enlarged to show individual clusters. Scale bar: 0.2 μm. Third column: Cluster maps from enlarged regions. Fourth column: Localization density maps show normalized relative density of the enlarged regions in the second column. (B-F) Quantitative analyses of the WT and YA clusters: (B) Hopkins index of WT and YA, n = 40 and n = 40; (C) Percentage of localizations in clusters, n = 72 and 77; (D) Average cluster diameters, n = 72 and 77; (E) Relative density, n = 71 and 76; (F) total density of the region, n = 72 and 77. (G) First column: Cross-section (Δz = 600 nm) of SMLM images of the FLAG-tagged NiV-F-WT treated without (NC) and with pitstop2 (pitstop2) on HeLa cell membrane. Scale bar: 1 μm. Second column: The yellow boxed region in the first column is enlarged to show individual clusters. Scale bar: 0.2 μm. Third column: Cluster maps from enlarged regions. Fourth column: Localization density maps show normalized relative density of the enlarged regions in the second column. (H-L) Quantitative analyses of NiV-F without (NC) and with pitstop2 (pitstop2): (H) Hopkins index, n = 40 and n = 40; (I) Percentage of localizations in clusters, n = 82 and 85; (J) Average cluster diameters, n = 82 and 81; (K) Relative density, n = 82 and 81; (L) total density of the region, n = 82 and 81. Bars represent mean ± SD. p value was obtained using Mann-Whitney test. ns: p > 0.05; * p<0.01; ** p<0.001; *** p<0.0001. Sample size n is the number of total regions from 4-9 cells.*

## Discussion.

Here we used SMLM to resolve the arrangement and organization of NiV-F on the biological membranes at a precision of 10 nm. Our data supports the following conclusions: 1) NiV-F is

390 organized into nanoclusters on the biological membranes and this organization is independent
391 of the protein expression level or endosomal cleavage; 2) the NiV-F nano-organization is
392 susceptible to mutations at the trimer interface on the NiV-F ectodomain and the putative
393 oligomerization motif on the transmembrane domain; 3) NiV-F sequestered in nanoclusters
394 favors membrane fusion activation; 4) the interactions among NiV-F, the AP-2 complex, and the
395 clathrin coat assembly stabilize the NiV-F clusters. We propose that the NiV-F nanoclusters are
396 the fundamental unit of the NiV fusion machinery, and this organization facilitates membrane
397 fusion triggering by a mixed population of NiV-F molecules with varied degrees of cleavage and
398 opportunities of interacting with NiV-G/receptor complex.

399 The nano-organization of NiV-F informs the coordinated membrane fusion triggering by a mixed
400 population of NiV-F. This notion is supported by the following observations from this and
401 previous studies: 1) NiV-F molecules form distinctive, regular-sized nanoclusters on the cell and
402 virus membranes (Fig. 1A-E); 2) the cleaved, active F co-exist with the noncleaved, inactive F in
403 a nanocluster, as suggested by that the NiV-F nanoclusters are resistant to the cathepsin
404 inhibitor, E64d (Fig. 2); 3) the NiV-F and G are segregated into different clusters[11]; and 4) the
405 full-length NiV-F and -G proteins do not show stable interactions either before or after ephrinB2
406 activation[12]. These observations indicate that the NiV-F triggering may be a result of transient
407 interactions between the F molecules at the edge of the clusters with the adjacent ephrinB2/G
408 complex. Moreover, we observed that the NiV-F sequestering into clusters is favorable for
409 membrane fusion activation (Fig. 3, 4, and 5), highlighting the importance of the spatial
410 arrangement of NiV-F in its fusion activity. Therefore, it is likely that the triggered, fusion-active
411 NiV-F at the cluster peripheral can facilitate other F molecules in the same cluster to fulfill the
412 conformational changes, and thus maximize the energy to merge the opposing membranes. In
413 contrast, the correlation between the clustering pattern of NiV-F and its incorporation into virions
414 is not obvious. Although the YA and LI4A mutants that showed aberrant clusters cannot
415 incorporate into VSV/NiV pseudovirions (Fig. S6F and S7F), the clustering-deficient hexameric
416 interface mutants L53D and V108D were incorporated into VLPs (Fig. 4A) and VSV/NiV
417 pseudovirisons (Fig. S4F) comparable to that of NiV-F-WT. Therefore, the significance of NiV-F
418 clustering for assembly and budding of the virions may be context-dependent.

419 A previous study revealed a hexamer-of-trimer assembly of soluble, GCN4-decorated, prefusion
420 NiV-F. Using SMLM, we estimated that the NiV-F clusters on the cell plasma membrane had a
421 diameter between 24-26 nm (Fig. 1F). This estimation agrees with the size of the hexameric
422 soluble NiV-F-GCN4 assemblies[10]. Notably, the density of clusters (Fig. 1I), but not the size and
423 localization density of individual clusters (Fig. 1G and H), is affected by the surface expression
424 levels of NiV-F, implying that the NiV-F clusters are highly regulated. A collaborative effort of
425 multiple copies of viral envelope proteins is favorable for receptor binding and overcoming the
426 energy barrier for membrane fusion. Nanoclusters formed by viral glycoproteins have been
427 observed for HIV-1[29,30], Herpes virus[31], and Influenza virus[32]. The viral restriction factor, serine
428 incorporator protein 5 (SERINC5), inhibits HIV-1 fusion by disrupting the HIV env nanoclusters,
429 highlighting the importance of the nanoclusters in the function of the viral glycoproteins[33]. More
430 interestingly, the NiV-F distribution becomes more dispersed, characterized by smaller and less
431 dense clusters, upon the mutation of two key residues, L53 and V108, at the hexameric
432 interface, suggesting that the NiV-F clusters are likely to be the hexamer-of-trimer assemblies
433 on the cell and viral membranes (Fig. 3 and 4).

434 The hexamer-of-trimer NiV-F is observed on the VLP surface by electron tomography[10]. The
435 NiV-F hexamer-of-trimers are arranged into a soccer ball-like structure, with one trimer being
436 part of multiple hexamer-of-trimers. Nonetheless, the hexagonal lattice has been reported for
437 heamagglutinin-esterase-fusion (HEF) proteins on the surface of the influenza C virus[34] and Env
438 glycoprotein on the Foamy virus[35]. The sharing of one trimer among hexamer-of-trimers and
439 conformational arrangements in the ectodomain of viral glycoproteins were shown to stabilize
440 the contacts for lattice formation[10,34,35]. In our study, the NiV-F clusters observed on the cell
441 plasma membrane are more likely to be individual hexamer-of-trimers estimated by size (Fig. 1).
442 We speculate that the formation of the hexagonal lattice may be a result of increased
443 concentration of NiV-F on VLP membrane. A study on Measles virus shows only limited high
444 order of MeV-F assemblies at some virus assembly sites in recMeV-(H-118 ∇41×) cells[36],
445 however, we have not observed increased NiV-F localizations at NiV-M positive membrane
446 domains on the cell body of NiV-M, F, and G co-expression PK13 cells[8]. Therefore, the
447 formation of NiV-F lattice on the VLP membrane may occur either at a late stage of virus
448 assembly or after budding. Additionally, cellular factors may also play a role in maintaining
449 individual NiV-F hexamer-of-trimers on the plasma membrane, as a proteomic analysis reveals
450 that NiV-F is an interacting partner of many vesicular trafficking and actin cytoskeleton
451 factors[26,28].

452 We also identified that the endosomal components as key host factors in maintaining the NiV-F
453 nano-organization on the cell membrane. Our data suggest that both the disruption of the F/AP-
454 2 interaction and the inhibition of clathrin assembly by pitstop2 result in dispersed NiV-F
455 distribution. AP-2 is the key adaptor of clathrin-mediated endocytosis. It binds cargo and
456 PtdIns(4,5)$P_2$ -containing membrane via multiple interface, and undergoes conformational
457 changes to append to the clathrin lattice[25,37]. Our data indicate that AP-2-NiV-F interaction can
458 enrich and strengthen the F nanoclusters (Fig. 6A-F and Fig. S7H), and potentially facilitate the
459 uptake of NiV-F by endocytosis for endosomal cleavage and activation. It is reported that the
460 clustering of CD44, modulated by *N*-glycosylations, facilitates the uptake of CD44 by
461 endocytosis. Furthermore, the assembly of the clathrin coat at the plasma membrane may also
462 strengthen the F clusters, because pitstop2 that inhibits the clathrin-coat assembly by blocking
463 the clathrin terminal domain[25] prevents the cluster formation of NiV-F. It is plausible that both
464 clathrin and AP-2 facilitate NiV-F clustering on cell and virus membranes because of the similar
465 organization of F on virus and cell membranes and the presence of clathrin and AP-2 in
466 VLPs[26,28].

467 In conclusion, our observations provide direct evidence on the nano-organization and
468 distribution of NiV-F on the cell and viral membranes and shed lights to the fusion activation
469 mechanisms. Therefore, it would be critical to elucidate host factors that maintain NiV-F clusters
470 and the interacting motif in NiV-F, which may represent a new therapeutic strategy for NiV
471 infections. It would also be interesting to analyze the reorganization of the NiV-F clusters upon
472 triggering by the NiV-G/receptor complex on live cell membranes by combining single-molecule
473 imaging and the supported lipid bilayer technologies[12]. Additionally, a precise stoichiometry of
474 individual NiV-F clusters on the cell and virus membranes could facilitate the vaccine design.

475

476

477

478 **Materials and Methods.**

| Reagent type | Designation | Source or reference | Identifiers | Additional information |
|---|---|---|---|---|
| Cell line | HEK293T | ATCC | CRL-3216 | |
| Cell line | PK13 | ATCC | CRL-6489 | |
| Cell line | HeLa | ATCC | CCL-2 | |
| Cell line | Vero | ATCC | CCL-81 | |
| DNA plasmid | NiV-F-FLAG and mutants | This paper | | The FLAG tag was inserted after residue 104 of the codon-optimized NiV-F (GenBank accession no. AY816748.1). The hexameric interface mutants (Fig. 3)[10], LI4A mutant (Fig. 5)[21], and YA mutant (Fig. 6)[6], were constructed as previously published. |
| DNA plasmid | NiV-F-HA | This paper | | The HA tag was inserted after residue 104 of the codon-optimized NiV-F (GenBank accession no. AY816748.1). |
| DNA plasmid | NiV-G-HA | Liu et al. 2018[11] | | |
| DNA plasmid | NiV-M-GFP | Liu et al. 2018, Wang et al. 2010 [11,38] | | The GFP gene was fused to the N-terminus of NiV-M gene (GenBank accession no. EU480491.1) |
| DNA plasmid | AP2µ2-mCherry | Christien Merrifield | Addgene 27672 | |
| DNA plasmid | Untagged NiV-F | | | Codon-optimized NiV-F (GenBank accession no. AY816748.1). |
| DNA plasmid | NiV-F-AU1 | | | The AU1 tag was inserted at the C terminal of the codon-optimized NiV-F (GenBank |

| | | | | |
|---|---|---|---|---|
| | | | | accession no. AY816748.1). |
| DNA plasmid | NiV-M-β-lactamase | Wolf et al., 2009[16] Landowski et al., 2014[17] | | The β-lactamase gene was fused to the N-terminus of NiV-M gene (GenBank accession no. EU480491.1) |
| Chemical compounds, drug | E64d | Sigma-Aldrich | E8640-250UG | 20uM |
| Chemical compounds, drug | Pitstop2 | Sigma-Aldrich | SML1169-5MG | 30uM |
| Chemical compounds, drug | Tris | EMD Millipore | 648311-1KG | 50 mM for TN buffer |
| Chemical compounds, drug | NaCl | Sigma-Aldrich | S9888-1KG | 10 mM for TN buffer |
| Chemical compounds, drug | Glucose oxidase | Sigma-Aldrich | G2133-50KU | 0.5 mg/ml for imaging buffer |
| Chemical compounds, drug | Catalase | Sigma-Aldrich | C100 | 40 µg/ml for imaging buffer |
| Chemical compounds, drug | Mercapto ethylamine (MEA) | Sigma-Aldrich | 30070-10G | 50 mM for SMLM imaging buffer |
| Chemical compounds, drug | HEPES | Fisher Scientific | 15-630-080 | 25 mM for fusion buffer |
| Chemical compounds, drug | Glutamine | Fisher Scientific | 25-030-081 | 2 mM for fusion buffer |
| Chemical compounds, drug | $CaCl_2$ | Sigma-Aldrich | C7902 | 1 mM for fusion buffer |
| Chemical compounds, drug | Probenecid | Sigma-Aldrich | P8761-25G | 2.5 mM for fusion buffer |
| Chemical compounds, drug | Solution D | Fisher Scientific | K1156 | 1:20 for Entry kinetics loading solution |
| Antibody | Anti-FLAG mouse monoclonal | Sigma-Aldrich | F1804 | IF, SMLM: 1:100, Flow: 1:200; WB: 1:500-1:5,000 |
| Antibody | Anti-HA rabbit polyclonal antibody | Biolegend | 902301 | IF: 1:900 WB: 1:2,000 |

| | | | | |
|---|---|---|---|---|
| Antibody | Anti-GFP goat polyclonal antibody | Abcam | Ab5450 | WB: 1:1000 |
| Antibody | Anti-mCherry rabbit polyclonal antibody | Abcam | Ab167453 | WB: 1:2000 |
| Antibody | Anti-β-lactamase mouse monoclonal | Santa Cruz Biotechnology | Sc-66062 | WB: 1:1000 |
| Antibody | Anti-mouse donkey polyclonal antibody, Alexa Fluor® 647 conjugated | Invitrogen | A31571 | IF and SMLM: 1:400 |
| Antibody | Anti-rabbit donkey polyclonal antibody, Alexa Fluor® 488 conjugated | Invitrogen | A21206 | IF: 1:400 |
| Antibody | Anti-mouse donkey polyclonal antibody, Alexa Fluor® 488 conjugated | Invitrogen | A21202 | Flow: 1:400 |
| Antibody | Anti-goat donkey polyclonal antibody, HRP conjugated | Jackson Immunoresearch | 705-035-147 | WB: 1:5,000 |
| Antibody | Anti-mouse goat polyclonal antibody, HRP conjugated | Biorad | 1705047 | WB: 1:5,000 |
| Antibody | Anti-rabbit goat polyclonal antibody, HRP conjugated | Biorad | 1706515 | WB: 1:5,000 |
| Commercial assays and kits | μMACS anti-DYKDDDDK starting kit | Miltenyi Biotec | 130-101-636 | |
| Commercial assays and kits | Renilla Luciferase Assay System | Promega | E2820 | |
| Commercial assays and kits | LiveBLAzer™ FRET-B/G Loading Kit with CCF2-AM | Invitrogen | K1032 | |

| | | | | |
|---|---|---|---|---|
| Commercial assays and kits | QIAamp Viral RNA Kits for RNA Extraction | QIAGEN | 52904 | |
| Commercial assays and kits | SuperScript™ III First-Strand Synthesis System | Invitrogen | 18080051 | |
| software | SMLM image reconstruction | Liu et al. 2018[11] | | MATLAB Codes are available upon request. |
| software | ClusDoc | Pageon et al. 2015[15] | | Codes were modified to process the data generated in the custom-built SMLM microscope. |
| software | OPTICS [18] | This paper | | C++ Codes are available upon request. |
| software | One-dimensional convolutional neural network (1D CNN) | This paper | | PYTHON Codes are available upon request. |
| software | Prism Graphpad | Dotmatics | | |
| software | Flowjo | BD | | |

Cell lines and plasmids.

PK13, HeLa, Vero and HEK293T cells were cultured at 37°C and 5% $CO_2$ in DMEM (Sigma-Aldrich, D6429) complemented with 10% fetal bovine serum (Invitrogen, 12483-020). Cells were passaged using phosphate-buffered saline (PBS, Invitrogen, 10010-049) and 0.25% Trypsin-EDTA solution (Invitrogen, 25002-072). Cells were monitored routinely for mycoplasma contamination using a mycoplasma detection PCR kit (ABM, G238). A FLAG (NiV-F-FLAG) or HA (NiV-F-HA) tag was inserted after residue 104 of codon-optimized NiV-F in pcDNA3.1 vector. An AU1(NiV-F-AU1) tag was inserted at the C-terminal of codon-optimized NiV-F in pCAGGS vector. The untagged NiV-F does not contain any epitope tag. NiV-F-YA, L53D, V108D, Q393L, and LI4A were produced by site-directed mutagenesis using the NiV-F-FLAG in pcDNA3.1 vector as a template[6,10,21]. AP2μ2-mcherry plasmid is a gift from Christien Merrifield (Addgene # 27672). The HA-tagged NiV-G, GFP-tagged NiV-M, and β-lactamase-NiV-M were constructed previously[7,16,38].

Immunofluorescence for SMLM.

For SMLM imaging on cells, $1\times10^5$ PK13 or HeLa cells were seeded on coverslips (Marienfeld #1.5H, 18 mm) coated with 2.5 μg fibronectin (Sigma-Aldrich, F4759-2 mg) in a 12-well plate, and transfected with 1 μg NiV-F variants using lipofectamine 3000 (Invitrogen, L3000015) on the following day. E64d was dissolved in methanol and pitstop2 in DMSO as recommended by the manufacturer. E64d was added to cells at 3 hrs post-transfection for a total treatment time of 15 hrs. Pitstop2 was added to cells at 10 hrs post-transfection for a total treatment time of 8 hrs. At 18 hrs post-transfection, cells were fixed with PBS containing 4% paraformaldehyde (PFA;

501 Electron Microscopy Sciences; 50980487) and 0.2% glutaraldehyde (Sigma-Aldrich, G5882-50
502 ml) for 90 min at room temperature. Cells were treated with signal enhancer image-IT-Fx (Life
503 Technologies, I36933) for 30 min at room temperature, and then blocked using BlockAid (Life
504 Technologies, B10710) for 1 hr at room temperature. The FLAG-tagged NiV-F and mutants were
505 detected by the anti-FLAG mouse monoclonal antibody (Sigma-Aldrich, F1804) and an Alexa
506 Fluor® 647 conjugated donkey anti-mouse secondary antibody (Invitrogen, A31571). Cells were
507 incubated with primary antibody overnight at 4°C, and then with the secondary antibody for 1 hr
508 at room temperature. Each antibody incubation is followed by five PBS washes, 5 min each
509 time. Cells were then fixed in PBS containing 4% PFA for 10 min at room temperature.

510 SMLM setup, imaging, and data analysis.

511 SMLM setup. Imaging was performed on a custom-built SMLM. Briefly, the microscope was built
512 upon an apochromatic TIRF oil-immersion objective lens (Nikon, 60x; numerical aperture 1.49).
513 Four lasers were used for excitation: a 639 nm laser (MRL-FN-639, 500 mW) for exciting Alexa
514 Fluor® 647, a 532 nm laser (MGL-III-532-300 mW) for exciting cy3B, a 488 nm laser (MBL-F-
515 473-300 mW) for exciting GFP, and a 405 nm laser (MDL-III-405-100 mW) for reactivating Alexa
516 Fluor 647 and cy3B. For SMLM imaging, the exciting and reactivating lasers were combined into
517 a single path using dichroic mirrors and then expanded and collimated using a beam expander.
518 The incident light beam was focused on the back focal plane of the objective lens. A translation
519 stage allowed the beam to be shifted between the center and edge of the objective lens so that
520 the incident light emerging from the objective lens reaches the sample at various angles. For
521 SMLM imaging of NiV-F at the cell and virus membranes at the cell-coverslip contact, the
522 incident angle of the illumination light was adjusted to near or greater than the critical angle of
523 the water-glass interface to allow total internal reflection and ensure low background
524 fluorescence for single fluorophore detection[39]. The emission fluorescence was separated using
525 appropriate dichroic mirrors and filters (Semrock) and detected by electron-multiplying charge-
526 coupled devices (EMCCD; Ixon, Andor). The full width at half maxima of the image of the point
527 spread function was magnified in size to ~3 camera pixels (106 nm per pixel), ensuring the
528 optimal fluorophore localization[39]. A feedback loop, composed of a tracking camera (Andor Zyla
529 SCOMS camera) and a computer-controlled piezo stage (Thorlabs 3-Axis NanoMax 300), was
530 employed to control the sample drift to <1 nm laterally and 2.5 nm axially[40].

531 Before SMLM imaging, fluorescence beads (Life technologies, F8799) were added to samples
532 as fiducial markers for drift control. Samples were immersed in imaging buffer [TN buffer (50
533 mM Tris (pH 8.0) and 10 mM NaCl), 0.5 mg/ml glucose oxidase, 40 μg/ml catalase, 10%
534 glucose, and 50 mM mercaptoethylamine (MEA)][14]. The expression level of the protein of
535 interest in individual cells was determined by measuring the average emission fluorescence
536 intensity of an area of 27×27 $\mu m^2$. To ensure sample stability during SMLM, a fiducial marker
537 was continuously tracked by the tracking camera. A brief procedure for SMLM imaging is
538 described as follows: 1) the sample was exposed to the imaging light beam [639 nm laser (1
539 $kW/cm^2$)] at a 90° incident angle to cause a subset of the fluorophores to switch to the
540 fluorescent state; 2) the incident light angle was adjusted close to or at the critical angle at the
541 water-glass interface to achieve total internal reflection; 3) a low density of activated
542 fluorophores were recorded to avoid fluorophore overlap; 4) another subset of fluorophores was
543 stochastically activated by exposure to the activation light (405 nm). This process was repeated
544 until 40,000 images were acquired. Custom-written software in MATLAB (Mathworks) was used
545 to identify activated fluorophores in each image, determine their precise locations by Gaussian

fitting, and reconstruct SMLM images[39]. Briefly, each image was first convolved with a Gaussian kernel to remove noise and background, and thresholded to search for local maxima. Next, two fitting steps were applied to determine the peak center position, the amplitude, and the width. Then, filtering and trail generation were combined to remove erroneous peaks and group multiple peaks originating from one activated fluorophore. Lastly, a list of fluorophore positions was reconstructed into a SMLM image. Clusters of NiV-F localizations on cell surface resolved by SMLM were identified and characterized using ClusDoC[15]. The min points and ε were set at 4 and 20, respectively.

VLP production and immunofluorescence.

To produce NiV VLPs, HEK293T cells were transfected by NiV-F-FLAG or mutants, NiV-G-HA, and NiV-M-GFP at a 9:1:5 ratio by using polyethylenimine (PEI) at 1 mg/ml (Polysciences, 23966-100). At 48hrs posttransfection, the supernatant of the cell culture was collected and subjected to ultracentrifugation on a 20% sucrose cushion at 125, 392 rcf for 90 min. The VLP-containing pellets were resuspended in 5% sucrose-NTE buffer. VLPs were bound to 2.5 µg fibronectin-coated 18 mm coverslips at 4°C overnight, followed by fixation using PBS containing 4% PFA and 0.2% glutaraldehyde. The protocols of immunofluorescence, SMLM setup, and SMLM imaging for cells were followed to stain and image NiV-F-FLAG and mutants on VLPs using SMLM. A widefield image of GFP was acquired and superimposed on the SMLM image of NiV-F. VLPs were identified as GFP-positive particles. The distribution of NiV-F localizations on VLPs was analyzed by using a custom-written OPTICS algorithm based on C++ and Point Cloud Library. Briefly, OPTICS segregates closely-situated data points into clusters from a 3D SMLM dataset[18]. OPTICS algorithm depends on two parameters: 1) $\varepsilon$ describes the radius for searching neighbors, and the number of neighbors of point p is called $N\varepsilon(p)$; 2) $minPts$ is a user-defined parameter; Point p is a core point if it has more than $minPts$ neighbors around it (including point $p$ itself). The core-distance and reachability-distance are calculated for cluster segregation. The core-distance is the Euclidean distance of the $minPtsth$ closest points to point $P$ (Equation (1)).

$$CoreDist_{\varepsilon,minPts}(p) = \begin{cases} UNDEFINED, if\ N_\varepsilon(p) < minPts, \\ minPts_{th}\ smallest\ distance\ in\ N_\varepsilon(p), otherwise \end{cases} \quad (1)$$

The reachability-distance of another Point $t$ to Point $p$ is either the Euclidean distance between point $t$ and point $p$ or the core-distance of $p$, whichever is bigger (Equation (2)).

$$ReachDist_{\varepsilon,minPts}(t,p) = \begin{cases} UNDEFINED, if\ N_\varepsilon(p) < minPts, \\ \max\left(CoreDist_{\varepsilon,minPts}(p), EudDist(p,t), otherwise\right. \end{cases} \quad (2)$$

The process begins by randomly selecting a point (point A). If the number of neighbors of point A is larger than the user-defined minPts (set at 10), the algorithm outputs point A without a reachability-distance value. Next, OPTICS obtains point A's nearest neighbor (point B) and outputs the B-A reachability-distance value. Point B is the new starting point. OPTICS recalculates the reachability-distance of all unprocessed neighbors of point B and selects the next point to process, as described above. This process repeats until all points in the dataset have been visited. The final output of OPTICS is a sequence of reachability-distances for each point.

The classification of the ordered sequence of reachability-distances was performed by using custom-written one-dimensional convolutional neural network (1D CNN) based on Python and Tensorflow. Briefly, CNN extracts features from OPTICS output dataset by using convolutional

586 layers for subsequent classification of the space information hidden in the OPTICS datasets. The
587 convolutional layers use a 1D sliding window to slide along the sequence data[41]. Each sliding
588 window captures local information and passes it to the next layer. Multiple CNN layers work
589 sequentially to build a high-dimensional representation of the dataset. A fully connected layer that
590 transforms high-dimensional features into classification results is achieved by CNN convolution.
591 We use t-SNE (t-distributed stochastic neighbor embedding) to reduce dimensionality on a trained
592 neural network layer for visualization in Fig 4C[42].

593 SDS-PAGE, and western blot analysis and co-immunoprecipitation.

594 For western blot analysis to confirm the expression of NiV-F-FLAG and mutants, HEK293T cells
595 were seeded in 6-well plate and transfected with 2.5 µg pcDNA3.1 empty vector, NiV-F-FLAG,
596 or mutants. At 28 or 48 hrs posttransfection, cells were lysed in RIPA buffer (Millipore-Sigma,
597 20-188) supplemented with protease inhibitor (Sigma-Aldrich, 11836170001) on ice for 30 min.
598 The cell lysates were collected after centrifuge at 16,000 ×g for 20 min at 4°C. The cell lysates
599 were supplemented with 1x SDS loading dye [60 mM Tris-HCl (pH=6.8); 2% SDS; 10% glycerol,
600 0.025% Brophenol blue] and 15 mM DTT (Thermo Scientific, R0861), and heated at 95°C for
601 denature. The denatured cell lysates were loaded into 10% polyacrylamide gels for SDS-PAGE.
602 Proteins were transferred to PVDF membrane, pore size 0.45 µm (Cytiva, GE10600021).
603 Membrane was blocked with 1% Bovine serum albumin (Sigma-Aldrich, A9647-50G) in PBS
604 and incubated with anti-FLAG mouse monoclonal antibody (Sigma-Aldrich, F1804). An HRP-
605 conjugated goat anti-mouse secondary antibody and the clarity Western ECL substrate (BioRad,
606 1705060) were used for protein detection. Images were acquired using Chemic Doc MP
607 Imaging System (BioRad).

608 For co-immunoprecipitation experiments, HEK293T cells were transfected with the following
609 combinations 1) 2.3 µg empty pcDNA 3.1 vector and 0.2 µg AP2µ2-mcherry, 2) 0.2 µg AP2µ2-
610 mcherry and 2.3 µg NiV-F-FLAG, and 3) 0.2 µg AP2µ2-mcherry and 2.3 µg NiV-F-YA. At 48 hrs
611 post-transfection, cells from 1 well of a 6-well plate were washed with PBS and lysed in 200 µl
612 lysis buffer provided with the µMACS DYKDDDDK isolation kit, and supplemented with protease
613 inhibitors. Cells were isolated on ice for 30 min. Cell debris was removed by centrifuge at
614 16,000 x g for 20 min at 4°C. 60 µl of cell lysate was set aside for immunoblot analysis, and the
615 rest was used for immunoprecipitation, as recommended by the manufacturer. 6 µl anti-
616 DYKDDDDK microbeads (Miltenyi Biotec, 130-101-591) were added to 140 µl cell lysates and
617 incubated for 30min on ice. µ columns (Miltenyi Biotec, 130-101-591) were prepared according
618 to the manufacturer's instructions. Lysate ran over the columns, and microbeads were washed
619 according to the manufacturer's instruction. 20 µl preheated elution buffer (95°C) was added to
620 the column before eluting the bound immunoprecipitated protein in 50 µl elution buffer. Elute
621 was separated by 10% SDS-PAGE, and proteins were immunoblotted by mouse anti-FLAG and
622 rabbit anti-mcherry primary antibodies. The HRP-conjugated goat anti-mouse and goat anti-
623 rabbit secondary antibodies were used for protein detection.

624 Flow cytometry.

625 HEK293T cells were seeded in 6-well plate and transfected with 2.5 µg pcDNA3.1 empty vector,
626 NiV-F-FLAG, or mutants. Cells were collected in 1 mL phosphate-buffered saline (PBS)
627 containing 10 mM EDTA after 28hrs post-transfection. The collected cells were incubated on ice
628 for 1 h with primary antibody mouse anti-flag diluted in 1:200. Samples were washed twice in
629 fluorescence-activated cell sorting (FACS) buffer (0.1% FBS with PBS). After washing, samples

were incubated with fluorescent anti-mouse Alexa Fluor 647 antibody 1:400 on ice for 45 min. After being washed twice again, samples were read on a flow cytometer (Attune® NxT™ Acoustic Focusing Cytometer, Thermo Fisher) The results were analyzed through FlowJo. The mean fluorescent intensities (MFI) were normalized to the MFIs of the NiV F-WT.

Cell-cell fusion.

HEK293T cells were seeded in the 12-well plate and transfected with 1μg total DNA of NiV-G and wt-F or mutant-F with a 3:1 ratio using Lipofectamine 3000. Cells were fixed with 4% PFA after 18 hrs post-transfection. Four or more nuclei within a common cytoplasm were considered syncytium. Syncytia were quantified by counting the number of nuclei in the syncytium per 10 × filed (5 fields are counted per group) under microscope TE2000U.

Viral entry kinetics assay.

HEK293T cells were loaded with CCF2-AM in the loading buffer by using a CCF2-AM loading kit (Invitrogen) and incubated at room temperature for 90 min. Loaded cells were washed three times and resuspended in 60 μl of cold fusion buffer (25mM HEPES, 2mMGlutamine, 1mM CaCl2, 2.5mM probenecid in HBSS). 110 μl fusion buffer, 10 μl of VLPs, and 60 μl of loaded cells were added into a black, clear-bottom 96-well plate on ice. The VLPs were allowed to attach to target cells at 4°C for 1 hr. Viral entry was measured by a Tecan fluorometer preheated to 37°C. Fluorescence was recorded every 3 min for 4 h. A blue-to-green (B/G) fluorescence ratio was determined for each well at each time point. The background control B/G ratio of VLPs expressing only MG and MF was then subtracted from each sample ratio as indicated, and the B/G ratio was plotted against time.

VSV/NiV pseudovirus production, quantitative PCR (qPCR), and viral entry quantification.

HEK293T cells in a 10 cm dish were transfected with NiV-F-Flag and NiV-G-HA. pCDNA3.1 vector was transfected as the negative control. At 18-20 hrs post-transfection, cells were infected by a recombinant VSV-ΔG-renilla luciferase virus in infection buffer (0.1% fetal bovine serum in PBS). After 48 hrs, the supernatant was collected and concentrated by ultra-centrifugation through a 20% sucrose cushion in NTE buffer at 125,000 × g at 4℃ for 90 min. The supernatant was removed and the pellet was re-suspended in the appropriate amount of 5% sucrose in NTE buffer. The expression levels of NiV-F and -G proteins in pseudoviruses were analyzed by Western blot, and the VSV genome copy number was quantified by qPCR. Briefly, the viral RNA of NiV/VSV pseudoviruses was extracted by using a Qiagen viral RNA extraction kit (QIAGEN, 52904), reverse transcribed to cDNA by the SuperScript III first-strand synthesis system (Invitrogen, 18080051). The VSV viral cDNA was quantified by using a qPCR Taqman probes (FAM-CGG TAT TTT TCC ATA ATT CAA GTA ATC TGC T-TAMRA) and the VSV-P plasmid was used as a standard to establish the standard curve. To quantify virus entry, Vero cells in a 96-well plate were infected using 10-fold serial virus dilutions. Infections were done for 2 h in infection buffer. After 24 hrs, the luciferase activity was measured using a Renilla luciferase assay kit (Promega E2810). The relative light units (RLUs) were plotted against the viral genome copy number per milliliter in GraphPad Prism.

**Acknowledgements.** We thank the multiscale imaging facility for instrument use. We thank Dr. Youssef Chebli at McGill University and Dr. David Scriven at the University of British Columbia for the support on laser scanning confocal microscopy and single-molecule imaging, respectively. **Funding.** This work is supported by funding from the Canadian Institutes of Health

Research to Q.L. (183861) and the Coronavirus Variants Rapid Response Network to Q.L. (175622). **Author contribution:** Conceptualization: Q.W. and Q.L.; Image acquisition: Q.W.; Data analysis and code writing: Q.W., J.L., and Q.L.; Functional analysis: Q.W., Y.L., V.K., G.L.M., J.W.; Resources: Q.L., Supervision: Q.L.; Funding Acquisition: Q.L.. Writing: original draft: Q.W., J.L., and Q.L.; revision: all authors. Competing Interests: The authors declare that they have no competing interests. Code, reagents, and data availability: Custom-written codes are deposited in GitHub or available upon request. Reagents can be provided by the corresponding author on a completed material transfer agreement. Requests for the reagents and data should be submitted to qian.liu3@mcgill.ca. **Declare of interests.** The authors declare no competing interests.

1. Navaratnarajah, C.K., Generous, A.R., Yousaf, I., and Cattaneo, R. (2020). Receptor-mediated cell entry of paramyxoviruses: Mechanisms, and consequences for tropism and pathogenesis. Journal of Biological Chemistry *295*, 2771–2786. https://doi.org/10.1074/jbc.REV119.009961.

2. Haas, G.D., and Lee, B. (2023). Paramyxoviruses from bats: changes in receptor specificity and their role in host adaptation. Current Opinion in Virology *58*, 101292. https://doi.org/10.1016/j.coviro.2022.101292.

3. Aditi, and Shariff, M. (2019). Nipah virus infection: A review. Epidemiology & Infection *147*, e95. https://doi.org/10.1017/S0950268819000086.

4. Thibault, P.A., Watkinson, R.E., Moreira-Soto, A., Drexler, J.F., and Lee, B. (2017). Zoonotic potential of emerging paramyxoviruses: knowns and unknowns. Adv Virus Res *98*, 1–55. https://doi.org/10.1016/bs.aivir.2016.12.001.

5. Diederich, S., Sauerhering, L., Weis, M., Altmeppen, H., Schaschke, N., Reinheckel, T., Erbar, S., and Maisner, A. (2012). Activation of the Nipah Virus Fusion Protein in MDCK Cells Is Mediated by Cathepsin B within the Endosome-Recycling Compartment. J Virol *86*, 3736–3745. https://doi.org/10.1128/JVI.06628-11.

6. Diederich, S., Moll, M., Klenk, H.-D., and Maisner, A. (2005). The Nipah Virus Fusion Protein Is Cleaved within the Endosomal Compartment *. Journal of Biological Chemistry *280*, 29899–29903. https://doi.org/10.1074/jbc.M504598200.

7. Negrete, O.A., Levroney, E.L., Aguilar, H.C., Bertolotti-Ciarlet, A., Nazarian, R., Tajyar, S., and Lee, B. (2005). EphrinB2 is the entry receptor for Nipah virus, an emergent deadly paramyxovirus. Nature *436*, 401–405. https://doi.org/10.1038/nature03838.

8. Liu, Q., Bradel-Tretheway, B., Monreal, A.I., Saludes, J.P., Lu, X., Nicola, A.V., and Aguilar, H.C. (2014). Nipah Virus Attachment Glycoprotein Stalk C-Terminal Region Links Receptor Binding to Fusion Triggering. J Virol *89*, 1838–1850. https://doi.org/10.1128/JVI.02277-14.

9. Liu, Q., Stone, J.A., Bradel-Tretheway, B., Dabundo, J., Montano, J.A.B., Santos-Montanez, J., Biering, S.B., Nicola, A.V., Iorio, R.M., and Lu, X. (2013). Unraveling a three-step spatiotemporal mechanism of triggering of receptor-induced Nipah virus fusion and cell entry. PLoS Pathog *9*, e1003770.

10. Xu, K., Chan, Y.-P., Bradel-Tretheway, B., Akyol-Ataman, Z., Zhu, Y., Dutta, S., Yan, L., Feng, Y., Wang, L.-F., Skiniotis, G., et al. (2015). Crystal Structure of the Pre-fusion Nipah

714 Virus Fusion Glycoprotein Reveals a Novel Hexamer-of-Trimers Assembly. PLoS Pathog *11*,
715 e1005322. https://doi.org/10.1371/journal.ppat.1005322.

716 11. Liu, Q., Chen, L., Aguilar, H.C., and Chou, K.C. (2018). A stochastic assembly model for
717 Nipah virus revealed by super-resolution microscopy. Nature Communications *9*, 3050.
718 https://doi.org/10.1038/s41467-018-05480-2.

719 12. Wong, J.J., Chen, Z., Chung, J.K., Groves, J.T., and Jardetzky, T.S. (2021). EphrinB2
720 clustering by Nipah virus G is required to activate and trap F intermediates at supported lipid
721 bilayer–cell interfaces. Sci. Adv. *7*, eabe1235. https://doi.org/10.1126/sciadv.abe1235.

722 13. Coelho, S., Baek, J., Graus, M.S., Halstead, J.M., Nicovich, P.R., Feher, K., Gandhi, H.,
723 Gooding, J.J., and Gaus, K. (2020). Ultraprecise single-molecule localization microscopy
724 enables in situ distance measurements in intact cells. Science Advances *6*, eaay8271.
725 https://doi.org/10.1126/sciadv.aay8271.

726 14. Dempsey, G.T., Vaughan, J.C., Chen, K.H., Bates, M., and Zhuang, X. (2011). Evaluation of
727 fluorophores for optimal performance in localization-based super-resolution imaging. Nature
728 Methods *8*, 1027–1036. https://doi.org/10.1038/nmeth.1768.

729 15. Pageon, S.V., Nicovich, P.R., Mollazade, M., Tabarin, T., and Gaus, K. (2016). Clus-DoC: a
730 combined cluster detection and colocalization analysis for single-molecule localization
731 microscopy data. Mol Biol Cell *27*, 3627–3636. https://doi.org/10.1091/mbc.E16-07-0478.

732 16. Wolf, M.C., Wang, Y., Freiberg, A.N., Aguilar, H.C., Holbrook, M.R., and Lee, B. (2009). A
733 catalytically and genetically optimized beta-lactamase-matrix based assay for sensitive,
734 specific, and higher throughput analysis of native henipavirus entry characteristics. Virol J *6*,
735 119. https://doi.org/10.1186/1743-422X-6-119.

736 17. Landowski, M., Dabundo, J., Liu, Q., Nicola, A.V., and Aguilar, H.C. (2014). Nipah Virion
737 Entry Kinetics, Composition, and Conformational Changes Determined by Enzymatic Virus-
738 Like Particles and New Flow Virometry Tools. J Virol *88*, 14197–14206.
739 https://doi.org/10.1128/JVI.01632-14.

740 18. Ankerst, M., Breunig, M.M., Kriegel, H.-P., and Sander, J. (1999). OPTICS: ordering points
741 to identify the clustering structure. SIGMOD Rec. *28*, 49–60.
742 https://doi.org/10.1145/304181.304187.

743 19. Kiranyaz, S., Avci, O., Abdeljaber, O., Ince, T., Gabbouj, M., and Inman, D.J. (2021). 1D
744 convolutional neural networks and applications: A survey. Mechanical Systems and Signal
745 Processing *151*, 107398. https://doi.org/10.1016/j.ymssp.2020.107398.

746 20. Barrett, C.T., and Dutch, R.E. (2020). Viral Membrane Fusion and the Transmembrane
747 Domain. Viruses *12*, 693. https://doi.org/10.3390/v12070693.

748 21. Webb, S., Nagy, T., Moseley, H., Fried, M., and Dutch, R. (2017). Hendra virus fusion
749 protein transmembrane domain contributes to pre-fusion protein stability. Journal of
750 Biological Chemistry *292*, 5685–5694. https://doi.org/10.1074/jbc.M117.777235.

751 22. Bonifacino, J.S., and Neefjes, J. (2017). Moving and positioning the endolysosomal system.
752 Curr Opin Cell Biol *47*, 1–8. https://doi.org/10.1016/j.ceb.2017.01.008.

23. Bonifacino, J.S., and Traub, L.M. (2003). Signals for sorting of transmembrane proteins to endosomes and lysosomes. Annu Rev Biochem *72*, 395–447. https://doi.org/10.1146/annurev.biochem.72.121801.161800.

24. Mattera, R., Farías, G.G., Mardones, G.A., and Bonifacino, J.S. (2014). Co-assembly of Viral Envelope Glycoproteins Regulates Their Polarized Sorting in Neurons. PLOS Pathogens *10*, e1004107. https://doi.org/10.1371/journal.ppat.1004107.

25. von Kleist, L., Stahlschmidt, W., Bulut, H., Gromova, K., Puchkov, D., Robertson, M.J., MacGregor, K.A., Tomilin, N., Pechstein, A., Chau, N., et al. (2011). Role of the Clathrin Terminal Domain in Regulating Coated Pit Dynamics Revealed by Small Molecule Inhibition. Cell *146*, 471–484. https://doi.org/10.1016/j.cell.2011.06.025.

26. Johnston, G.P., Bradel-Tretheway, B., Piehowski, P.D., Brewer, H.M., Lee, B.N.R., Usher, N.T., Zamora, J.L.R., Ortega, V., Contreras, E.M., Teuton, J.R., et al. (2019). Nipah Virus-Like Particle Egress Is Modulated by Cytoskeletal and Vesicular Trafficking Pathways: a Validated Particle Proteomics Analysis. mSystems *4*, 10.1128/msystems.00194-19. https://doi.org/10.1128/msystems.00194-19.

27. Pentecost, M., Vashisht, A.A., Lester, T., Voros, T., Beaty, S.M., Park, A., Wang, Y.E., Yun, T.E., Freiberg, A.N., Wohlschlegel, J.A., et al. (2015). Evidence for ubiquitin-regulated nuclear and subnuclear trafficking among Paramyxovirinae matrix proteins. PLoS Pathog *11*, e1004739. https://doi.org/10.1371/journal.ppat.1004739.

28. Vera-Velasco, N.M., García-Murria, M.J., Sánchez Del Pino, M.M., Mingarro, I., and Martinez-Gil, L. (2018). Proteomic composition of Nipah virus-like particles. J Proteomics *172*, 190–200. https://doi.org/10.1016/j.jprot.2017.10.012.

29. Chojnacki, J., and Eggeling, C. (2018). Super-resolution fluorescence microscopy studies of human immunodeficiency virus. Retrovirology *15*, 41. https://doi.org/10.1186/s12977-018-0424-3.

30. Muranyi, W., Malkusch, S., Müller, B., Heilemann, M., and Kräusslich, H.-G. (2013). Super-Resolution Microscopy Reveals Specific Recruitment of HIV-1 Envelope Proteins to Viral Assembly Sites Dependent on the Envelope C-Terminal Tail. PLOS Pathogens *9*, e1003198. https://doi.org/10.1371/journal.ppat.1003198.

31. Laine, R.F., Goodfellow, G., Young, L.J., Travers, J., Carroll, D., Dibben, O., Bright, H., and Kaminski, C.F. (2018). Structured illumination microscopy combined with machine learning enables the high throughput analysis and classification of virus structure. eLife *7*, e40183. https://doi.org/10.7554/eLife.40183.

32. McMahon, A., Andrews, R., Groves, D., Ghani, S.V., Cordes, T., Kapanidis, A.N., and Robb, N.C. (2023). High-throughput super-resolution analysis of influenza virus pleomorphism reveals insights into viral spatial organization. PLOS Pathogens *19*, e1011484. https://doi.org/10.1371/journal.ppat.1011484.

33. Chen, Y.-C., Sood, C., Marin, M., Aaron, J., Gratton, E., Salaita, K., and Melikyan, G.B. (2020). Super-Resolution Fluorescence Imaging Reveals That Serine Incorporator Protein 5 Inhibits Human Immunodeficiency Virus Fusion by Disrupting Envelope Glycoprotein Clusters. ACS Nano *14*, 10929–10943. https://doi.org/10.1021/acsnano.0c02699.

794 34. Halldorsson, S., Sader, K., Turner, J., Calder, L.J., and Rosenthal, P.B. (2021). In situ
795 structure and organization of the influenza C virus surface glycoprotein. Nat Commun *12*,
796 1694. https://doi.org/10.1038/s41467-021-21818-9.

797 35. Effantin, G., Estrozi, L.F., Aschman, N., Renesto, P., Stanke, N., Lindemann, D., Schoehn,
798 G., and Weissenhorn, W. (2016). Cryo-electron Microscopy Structure of the Native
799 Prototype Foamy Virus Glycoprotein and Virus Architecture. PLoS Pathog *12*, e1005721.
800 https://doi.org/10.1371/journal.ppat.1005721.

801 36. Ke, Z., Strauss, J.D., Hampton, C.M., Brindley, M.A., Dillard, R.S., Leon, F., Lamb, K.M.,
802 Plemper, R.K., and Wright, E.R. (2018). Promotion of virus assembly and organization by
803 the measles virus matrix protein. Nat Commun *9*, 1736. https://doi.org/10.1038/s41467-018-
804 04058-2.

805 37. Kovtun, O., Dickson, V.K., Kelly, B.T., Owen, D.J., and Briggs, J.A.G. (2020). Architecture of
806 the AP2/clathrin coat on the membranes of clathrin-coated vesicles. Sci Adv *6*, eaba8381.
807 https://doi.org/10.1126/sciadv.aba8381.

808 38. Wang, Y.E., Park, A., Lake, M., Pentecost, M., Torres, B., Yun, T.E., Wolf, M.C., Holbrook,
809 M.R., Freiberg, A.N., and Lee, B. (2010). Ubiquitin-Regulated Nuclear-Cytoplasmic
810 Trafficking of the Nipah Virus Matrix Protein Is Important for Viral Budding. PLOS Pathogens
811 *6*, e1001186. https://doi.org/10.1371/journal.ppat.1001186.

812 39. Bates, M., Jones, S.A., and Zhuang, X. (2013). Stochastic Optical Reconstruction
813 Microscopy (STORM): A Method for Superresolution Fluorescence Imaging. Cold Spring
814 Harb Protoc *2013*, pdb.top075143. https://doi.org/10.1101/pdb.top075143.

815 40. Tafteh, R., Scriven, D.R.L., Moore, E.D.W., and Chou, K.C. (2016). Single molecule
816 localization deep within thick cells; a novel super-resolution microscope. J Biophotonics *9*,
817 155–160. https://doi.org/10.1002/jbio.201500140.

818 41. Yu, Y., Zhu, Y., Li, S., and Wan, D. (2014). Time Series Outlier Detection Based on Sliding
819 Window Prediction. Mathematical Problems in Engineering *2014*, 879736.
820 https://doi.org/10.1155/2014/879736.

821 42. The art of using t-SNE for single-cell transcriptomics | Nature Communications
822 https://www.nature.com/articles/s41467-019-13056-x.

823